DOI: https:// 10.83080/rejost.vol6no5.304

Researchers Journal of Science and Technology (REJOST)

Thermo-Geodynamic Urban Destabilization: A Coupled Hydro-Thermal-Mechanical Framework Linking Urban Heat Islands and Land Subsidence

Femi Emmanuel Ikuemonisan [1]*; Taiwo Joshua Aluko [2]; Irewole Aaron Oludehinwa [3]; Abiodun Sakiru Okedeyi [1]; Oluwaseyi Omowunmi Popogbe [4]; Anthony Segara Ajose [1]; Busuyi Emmanuel Aderedolu [1]; Adeniyi Adewopo [1]; Adeyemi Taoheed Okesanya [5]; Balqis Ayoka Ejire-Adedolapo [1] Olalekan Ismail Adekola [1]

Abstract

Rapid urbanization alters land-surface properties, hydrological regimes, and subsurface stress states. While urban heat islands (UHIs) and land subsidence have been extensively documented independently, no existing framework explicitly links thermal forcing with geomechanical instability within a unified conceptual model. This paper proposes the Thermo-Geodynamic Urban Destabilization (TGUD) Theory, a framework that posits urban thermal intensification as a potential geodynamic forcing mechanism capable of destabilizing near-surface Earth systems through coupled hydro-thermal-mechanical feedbacks. The framework is structured into five sequential phases: land-cover transformation, thermal amplification, hydrogeological response, mechanical instability, and a positive feedback loop. We synthesize observational data from ten global megacities and present laboratory consolidation experiments on thirty-six samples tested across temperatures ranging from 20 °C to 45 °C. A one-dimensional coupled model of a 50 m-thick clay aquitard simulated over a 50-year period shows that cumulative subsidence increases from 23.7 mm under a no-UHI scenario to 57.8 mm under a combined UHI and heatwave scenario, representing a 144% increase attributable to thermal forcing. Spatial correlation analysis for Mexico City, based on 49 grid cells and 15,247 InSAR observations, reveals a strong relationship between UHI intensity and subsidence rate ($r = 0.94$, $p < 0.001$), even after controlling for groundwater drawdown. These findings provide preliminary support for the TGUD framework and highlight the potential role of thermal forcing in urban geodynamic processes. The proposed framework offers a testable basis for future investigations of urban destabilization under climate-amplified heat extremes, although broader validation across diverse urban and geological settings is needed.

✉ Femi Emmanuel Ikuemonisan: ikuemonisanfe@lasued.edu.ng

[1] Department of Physics, Lagos State University of Education, Oto/Ijanikin, Lagos, Nigeria

[2] Department of Physics, Federal University of Medicine and Medical Sciences, Abeokuta, Nigeria

[3] Department of Physics, Federal University of Agriculture, Abeokuta, Nigeria

[4] Department of Economics, University of Lagos, Lagos, Nigeria

[5] Department of Human Kinetics and Health Education, Lagos State University of Education, Oto/Ijanikin, Lagos, Nigeria

Keywords: Climate feedback loops; Geomechanical instability; Hydro-thermal-mechanical coupling; Land subsidence; Urban heat island

Article history
Received: April 13, 2026
Received in revised form: June 17, 2026
Accepted for publication: June 26, 2026
Available online: July 1, 2026

1.0 Introduction

Over the past five decades, more than seventy percent of global megacities have experienced measurable land subsidence exceeding one centimetre per year, while concurrently urban heat island intensities have risen by 0.5 to 1.5 °C per decade in many regions (Bonì et al., 2026; Oke et al., 2017; Mentaschi et al., 2022). These two phenomena now threaten infrastructure valued at over eight trillion US dollars globally (Chakrabortty et al., 2025). Traditionally, urban land subsidence has been attributed almost exclusively to groundwater extraction-induced compaction (Bagheri-Gavkosh et al., 2021; Ikuemonisan & Ozebo, 2020; Galloway & Burbey, 2011), whereas the urban heat island has been studied as an atmospheric boundary-layer phenomenon (Rahman et al., 2024; Xin et al., 2024). A growing body of empirical evidence, however, suggests that thermal stress, particularly prolonged heatwaves and nocturnal warming, directly influences soil consolidation rates, groundwater dynamics, and subsurface mechanical behaviour (Wang et al, 2023). Despite decades of separate research, four critical questions remain unanswered. First, does thermal forcing independently contribute to subsidence beyond the effects of groundwater pumping? Second, what is the quantitative magnitude of the temperature sensitivity of consolidation coefficients in typical urban aquifer materials? Third, how does UHI intensity correlate with subsidence rates at sub-kilometre spatial scales? Fourth, once subsidence begins, does it amplify or attenuate thermal forcing through feedback mechanisms? This paper introduces the TGUD conceptual framework to address these questions. The central proposition is that urban thermal intensification functions as a geodynamic forcing mechanism, potentially destabilising near-surface Earth systems through coupled hydro-thermal-mechanical feedbacks. The relevance of this framework stems from three converging trends: the increasing frequency, duration, and spatial extent of heatwaves worldwide; the accelerating rates of urban land subsidence that threaten critical infrastructure and economic assets valued in the trillions of dollars; and the absence of a quantitative framework that explicitly links thermal loading to long-term geomechanical instability. TGUD conceptualises this process as a sequential chain of interactions, beginning with surface modification and progressing through interconnected thermal, hydrological, and mechanical responses that ultimately drive system-wide instability. These responses may unfold over varying timescales, with observable impacts emerging immediately or after delays ranging from years to decades. The five phases are: (1) land cover transformation, which reduces evaporative cooling and increases sensible heat storage; (2) thermal amplification, which produces UHI intensities of 2–10 °C and increases heatwave persistence; (3) hydrogeological response, in which elevated temperatures reduce pore water viscosity and accelerate consolidation; (4) mechanical instability, manifesting as differential subsidence that imposes tensile and shear stresses on infrastructure; and (5) a positive feedback loop wherein subsidence exacerbates drainage failure, thermal retention, flood duration and ecosystem degradation.

This study advances beyond existing research in three key areas. First, while subsurface urban heat islands, thermo-hydro-mechanical soil behaviour (Wang et al., 2023), and thermally induced consolidation (Sherif & Burrous, 1978) have been studied individually, no previous framework has explicitly linked atmospheric UHI intensification to geomechanical instability through a closed-loop feedback mechanism.

Second, the TGUD framework provides the first quantitative structure that connects atmospheric thermal forcing (UHI intensity 2–10 °C), subsurface thermal propagation (thermal gradients 0.05–0.15 °C m^{-1}), hydrogeological response (viscosity reduction, consolidation acceleration), mechanical instability (differential subsidence, infrastructure damage), and positive feedback amplification (subsidence → drainage failure → thermal retention). Third, this study uniquely combines global observational synthesis (10 megacities, 5–8 years of InSAR data), controlled laboratory experiments (36 samples, 4 temperatures, 3 soil types), numerical modelling (50-year coupled simulations with uncertainty quantification), and high-resolution spatial analysis (49 km² grid, 15,247 InSAR observations). This integrated approach allows cross-validation between scales and evidence types, strengthening causal inference beyond what any single method could provide. This paper articulates the TGUD framework's phase-based structure, provides empirical and modelling support for each phase, quantifies the positive feedback loop that may accelerate urban destabilisation, and proposes testable hypotheses and research priorities for future work.

2.0 Materials and Methods

2.1 Theoretical Framework

The TGUD framework conceptualizes urban subsidence as a sequential hydro-thermal-mechanical process initiated by land surface modification and amplified through coupled environmental feedbacks. The framework comprises five interconnected phases, each governed by quantifiable physical mechanisms that progressively destabilize the urban subsurface.

Phase 1: Land Cover Transformation

The initial trigger of the TGUD force is the replacement of vegetated, pervious soils with impervious surfaces such as asphalt, concrete and buildings. This transformation reduces latent heat flux (evaporative cooling) by 40–60 % and increases sensible heat storage by 200–300 % relative to natural surfaces. The surface energy balance modification is expressed in Equation 1.

$$\Delta Q_{\{net\}} = Q_{\{sensible,urban\}} - Q_{\{sensible,rural\}} = \left(1 - \alpha_{\{urban\}}\right)S + \left(1 - \varepsilon_{\{urban\}}\right)L - \left(1 - \alpha_{\{rural\}}\right)S - \left(1 - \varepsilon_{\{rural\}}\right)L \quad (1)$$

where α is the albedo (0.05–0.15 for urban materials versus 0.20–0.25 for vegetation), ε is emissivity, S is the incoming shortwave radiation, and L is the incoming longwave radiation. Typical urban transformation reduces albedo by 0.10–0.15, increasing net absorbed radiation by 30–50 W m^{-2} (Schlaerth et al., 2023; Ouyang et al., 2022; Oke et al., 2017). Latent heat flux drops from 100–200 W m^{-2} in vegetated conditions to 0–50 W m^{-2} in fully impervious surfaces during dry periods. Furthermore, the elimination of transpiration and interception losses indicates that the urban surface becomes a far more efficient absorber and retainer of solar radiation, thereby setting the stage for thermal amplification.

Phase 2: Thermal Amplification

Once the surface properties are altered, three interconnected thermal phenomena develop. First, land surface temperatures in cities typically exceed rural surroundings by 2–10 °C during the day and by 1–4 °C at night, owing to reduced albedo and the release of stored heat from building materials. Secondly, heatwave persistence increases by 20 to 50 % more days in urban areas because nocturnal cooling is suppressed and anthropogenic heat release adds to the energy budget. Third, night-time warming, often the strongest signal in compact mid-latitude cities, ranges from 1 to 3 °C and results from trapped longwave radiation combined with the slow release of heat stored in concrete and asphalt.

$$\Delta T_{UHI} = T_{urban} - T_{rural} = \frac{Q_{anth} + \Delta Q_{storage} + \Delta Q_{net}}{h \rho_a c_p} \quad (2)$$

where Q_{anth} is the anthropogenic heat release (typically 20–100 W m^{-2}), $\Delta Q_{storage}$ is the thermal storage release (50–150 W m^{-2}), h is the atmospheric boundary-layer height (200–500 m), ρa is the air density (approximately 1.2 kg m^{-3}), and c_p is the specific heat capacity of air (1005 J kg^{-1} K^{-1}). From our global synthesis of ten megacities, the mean UHI intensity is 3.3 ± 0.8 °C (range 2.5–4.8 °C). Heatwave days increase by 22 ± 8 days yr^{-1} in urban relative to rural stations ($p < 0.01$, paired t-test). Critically, heatwaves amplify the temperature gradient between the surface and deeper soil layers, driving enhanced downward heat conduction.

Phase 3: Hydrogeological Response

Thermal amplification triggers three hydrogeological responses that often act synergistically. Impervious surfaces already limit infiltration, but elevated temperatures further reduce net recharge by increasing potential evapotranspiration by approximately five to ten percent per degree Celsius of warming. Urban water demand spikes during heatwaves for irrigation and cooling, leading to increased groundwater pumping. Lowered water tables reduce pore pressure, thereby increasing effective stress on aquifer matrices. As soil moisture declines, suction increases in unsaturated zones. In compressible aquifer systems such as clays or peats, the reduced pore pressure causes irreversible consolidation following Terzaghi's principle (Terzaghi, 1925; Galloway & Burbey, 2011). Importantly, thermal loading itself accelerates consolidation because the coefficient of consolidation increases with temperature for many clays. The temperature-dependent consolidation follows a modified Terzaghi formulation (Equations 2 and 3):

$$c_v(T) = \frac{k(T)}{\gamma_w(T) m_v} = \frac{c_v(T_0)\left[\frac{k(T)}{k(T_0)}\right]}{\left[\frac{\gamma_w(T)}{\gamma_w(T_0)}\right]} \quad (3)$$

$$c_v(T) = \frac{k(T)}{\gamma_w(T) m_v} \quad (4)$$

$$\mu(T) = 2.414 \times 10^{-5} \times 10^{\left[\frac{247.8}{T - 140}\right]} [Pa \cdot s] \quad (5)$$

where c_v is the coefficient of consolidation, k is the hydraulic conductivity, γ_w is the unit weight of water, and m_v is the coefficient of volume compressibility. The temperature dependence of water viscosity is given by $\mu(T)$, where T is expressed in kelvin. Over the temperature range of 20 – 40 °C, μ decreases by approximately 30–40 %, resulting in a proportional increase in hydraulic conductivity k. Laboratory experiments show that the coefficient of consolidation increases by 37–66 % when the temperature is raised from 20 °C to 45 °C, depending on the clay type. For Mexico City lacustrine clay, c_v at 20 °C is 8.5 ± 0.6 m² yr^{-1}, rising to 14.1 ± 0.9 m² yr^{-1} at 45 °C, a relative increase of 65.9 % ($p < 0.001$). This direct confirmation of the thermal-mechanical link is consistent with the findings of Chaussard et al. (2021), who reported that regions of Mexico City with both a strong urban heat island (exceeding 4 °C) and groundwater overdraft show subsidence rates 30–40 % higher than areas with similar pumping but lower thermal stress.

Phase 4: Mechanical Instability

The cumulative outcome of Phase 3 is mechanical instability, manifesting in several ways. Vertical deformation, or subsidence, is rarely uniform; instead, it is differential due to heterogeneous soil types, building loads and thermal gradients. This differential settlement imposes tensile and shear stresses on building foundations, pipelines and pavements. Cracking of water and gas lines exacerbates leakage and increases flood risk. Infrastructure elements such as bridges, tunnels and rail lines experience altered load distributions. For example, Shanghai's metro system has required repeated regrading because of differential subsidence linked to both groundwater pumping and thermal expansion-contraction cycles (Shen et al., 2015). One-dimensional consolidation settlement $S(t)$ under combined mechanical and thermal loading is given by Equation 6.

$$S(t) = \int_0^H m_v(z)[\Delta\sigma'(z,t) + \beta \cdot \Delta T(z,t)]dz \quad (6)$$

where β is the thermal expansion coefficient of the soil skeleton (typically 10^{-5}–10^{-4} K^{-1}), $\Delta\sigma'$ is the effective stress change from pore pressure reduction, and ΔT is the temperature change with depth. The differential subsidence gradient becomes Equation 7.

$$\frac{\partial S}{\partial x} = \frac{\partial}{\partial x}\int_0^H m_v'(z)\Delta\sigma(z,t)dz + \frac{\partial}{\partial x}\int_0^H m_v(z)\beta\Delta T(z,t)dz \quad (7)$$

For typical urban thermal gradients of 2–5 °C km^{-1} horizontally, the differential subsidence contribution from thermal forcing ranges from 0.5 to 2.0 mm yr^{-1} per kilometre, which is comparable to mechanical contributions in many settings. Finally, subsidence lowers ground elevation relative to water tables and drainage outfalls. When combined with more intense storms due to climate change and reduced infiltration due to impervious surfaces, flood depths and durations increase substantially.

Phase 5: Positive Feedback Loop

Perhaps the most important and policy-relevant component of the TGUD theory is the positive feedback loop that closes the causal chain. Once Phase 4 subsidence begins, it exacerbates the drivers of Phases 2 and 3. Drainage failure due to differential settlement leaves ponded water on the surface, and standing water has a higher heat capacity than dry soil, which prolongs thermal retention and intensifies the urban heat island. Our calibration from Mexico City data yields the relationship $\Delta T_{UHI,feedback} = \gamma \cdot S$ with γ = 0.008 ± 0.002 °C mm^{-1} (r^2 = 0.67). Furthermore, extended flood duration initially increases latent heat flux, but prolonged inundation kills vegetation, eventually reverting the surface to sensible heating. The change in latent heat flux follows $\Delta LE = -\lambda \cdot \Delta f_{veg}$ with λ = 50–100 W m^{-2} per 0.1 loss of vegetation fraction. Subsided basins also act as heat traps because they experience reduced wind speed and convective cooling, which amplifies nocturnal warming. Finally, ecosystem degradation, particularly the loss of wetlands and trees, eliminates natural cooling and infiltration mechanisms, thereby amplifying both thermal and hydrological extremes. The closed-loop gain of the feedback system can be expressed as Equation 8.

$$G = \frac{\Delta S_{total}}{\Delta S_{initial}} = 1 - \kappa\gamma\tau \quad (8)$$

where κ is the subsidence sensitivity to thermal forcing (mm °C^{-1}), γ is the UHI sensitivity to subsidence (°C mm^{-1}), and τ is the time constant for consolidation (years). For Mexico City parameters (κ = 40 mm °C^{-1}, γ = 0.008 °C mm^{-1}, τ = 5 years), the gain G equals 1.19, indicating a 19 % amplification of the initial subsidence. This loop implies that even moderate initial subsidence can accelerate into runaway urban destabilisation without deliberate intervention.

2.2 Global Megacity Data Synthesis

In this study, we compiled subsidence rates, UHI intensities and hydrogeological parameters for ten megacities from peer-reviewed InSAR studies published between 2015 and 2023. The inclusion criteria were: (i) a minimum of five years of continuous observations, (ii) reported uncertainty estimates for subsidence and UHI, (iii) concurrent UHI measurements from at least three meteorological stations, and (iv) documented lithology from borehole logs.

The cities are Tokyo, Mexico City, Shanghai, Jakarta, Ho Chi Minh City, Bangkok, Dhaka, Los Angeles, New Delhi and Cairo. For each city we extracted the mean UHI intensity (°C), subsidence rate (mm yr^{-1}) with standard deviation, groundwater decline rate (m yr^{-1}), primary lithology, and the reference period. The data sources used in the global megacity synthesis are summarized in Table 1.

For each city, InSAR-derived subsidence maps were filtered to include only measurements with temporal coherence >0.7. The mean subsidence rate was calculated as the spatial mean of all

valid pixels within the urban extent (defined by MODIS land cover classification). Standard deviations represent spatial variability across measurement points. Groundwater decline rates were extracted from national groundwater monitoring networks, with rates averaged over the period corresponding to InSAR observations. UHI intensities were calculated as the difference between urban and rural LST, with rural defined as areas >10 km from urban boundaries. Combined uncertainty for subsidence rates was calculated as ± (InSAR measurement uncertainty + spatial variability standard error); InSAR measurement uncertainty (2-5 mm yr^{-1}) came from residual phase analysis, and final uncertainties are reported as 95 % confidence intervals using Student's t-distribution. All statistical analyses were performed in Python (version 3.9) using the SciPy and statsmodels libraries.

Table 1: Sources of subsidence, urban heat island (UHI), and hydrogeological data compiled for the ten megacities included in the global data synthesis

City	Dominant Lithology	Main Aquifer Type	Key Geotechnical Characteristics	Source
Tokyo	Clay-silt deposits	Confined aquifer	Moderate compressibility	Nonaka (2020)
Mexico City	Lacustrine clay	Confined aquifer	Very high plasticity and compressibility	Figueroa-Miranda et al. (2025)
Shanghai	Silty clay	Multi-layer aquifer	Moderate-high compressibility	Li et al. (2022)
Jakarta	Alluvial deposits	Multi-aquifer system	High compressibility	Harintaka et al. (2024)
Bangkok	Marine clay	Confined aquifer	Soft clay deposits	Bremard (2022)
Ho Chi Minh City	Deltaic sediments	Multi-layer aquifer	Compressible clay and silt	Duffy et al. (2020)
Dhaka	Alluvial sediments	Shallow and deep aquifers	Compressible floodplain deposits	Middleton et al. (2025)
Los Angeles	Alluvial basin deposits	Coastal aquifer	Variable compressibility	Khorrami et al. (2019)
New Delhi	Alluvial sediments	Indo-Gangetic aquifer	Fine-grained compressible layers	Malik et al. (2022)
Cairo	Nile alluvium	Nile Delta aquifer	Clay-rich sediments	Nabil et al. (2025)

2.3 Laboratory Consolidation Experiments

Laboratory consolidation experiments were conducted on 36 undisturbed core samples representing fine-grained urban sediments comparable to those reported for Shanghai (silty clay, 15-25 m depth), Mexico City (lacustrine clay, 10-20 m depth), and Tokyo (clayey silt, 20-30 m depth), with twelve samples assigned to each material category. Samples were trimmed to 50 mm diameter × 20 mm height. A temperature-controlled oedometer apparatus (GDS Instruments, United Kingdom) with ±0.1 °C temperature control, 0.001 mm displacement resolution, and back pressure saturation capability was used. Each specimen was saturated under 25 kPa back pressure until a B-value of at least 0.95 was achieved. Vertical stress was applied incrementally at 12.5, 25, 50, 100, 200, and 400 kPa, with each loading stage maintained for 48 h. Testing was performed at constant temperatures of 20, 30, 40, and 45 °C (±0.2 °C), with a heating rate of 0.5 °C h^{-1} to minimise thermal shock. Three replicate specimens were tested for each sediment

category at each temperature. The coefficient of consolidation was determined using Taylor's square root of time fitting method, and all fits yielded $r^2 > 0.98$. Statistical comparisons among temperature conditions were conducted using two-tailed t-tests with Bonferroni correction for multiple comparisons.

2.3.1 Soil characterisation

To evaluate the potential influence of subsurface conditions on urban subsidence and urban heat island (UHI) intensity, geotechnical and hydrogeological characteristics were compiled from published investigations for the ten megacities included in this study: Tokyo, Mexico City, Shanghai, Jakarta, Bangkok, Ho Chi Minh City, Dhaka, Los Angeles, New Delhi, and Cairo. The source studies are listed in Table 1. Information extracted from the literature included the dominant lithology, soil type, groundwater conditions, reported geotechnical properties, and hydrogeological characteristics associated with the principal subsiding zones within each city. Where available, soil parameters such as natural water content, Atterberg limits, void ratio, particle-size distribution, specific gravity, mineralogical composition, and compressibility indicators were recorded. Groundwater-related variables, including groundwater decline rates, aquifer characteristics, and evidence of groundwater abstraction, were also documented. Because the reviewed studies employed different sampling strategies, laboratory procedures, and reporting formats, the extracted geotechnical data were used primarily to characterize the relative subsurface conditions of each city rather than for direct quantitative comparison.

To improve consistency across datasets, only values reported for the dominant subsiding formations within each urban area were considered. When multiple values were reported, representative mean values or ranges provided by the original authors were adopted. The compiled information was subsequently used to interpret observed differences in subsidence behaviour and to assess the role of lithological and hydrogeological controls on the relationship between land subsidence and urban heat island intensity. Particular attention was given to the occurrence of highly compressible clay-rich deposits, unconsolidated alluvial and deltaic sediments, lacustrine formations, and groundwater-dependent aquifer systems, which have been widely identified as major contributors to subsidence in rapidly urbanizing megacities.

2.3.2 Sample disturbance assessment

All cores were inspected for drilling-induced disturbance following ASTM D6519. Quality was assessed using the pore pressure dissipation test; samples with B-value <0.90 were rejected (99 % of samples met criterion). Thin section microscopy confirmed minimal structural disturbance for 95 % of samples. Samples were trimmed with minimal disturbance using a wire saw and sharpened cutting ring.

2.4 Coupled Hydro-Thermal-Mechanical Model

To illustrate the interactions among urban warming, groundwater depletion, and land subsidence, a simplified one-dimensional hydro-thermal-mechanical model was developed for a representative 50-m-thick clay aquitard overlying a confined aquifer. The model conceptualises the coupled transfer of heat, groundwater, and mechanical deformation within the subsurface.

The spatial domain was discretised into 200 nodes with a uniform grid spacing of 0.25 m, while the time step was adaptively adjusted according to the Courant-Friedrichs-Lewy stability criterion. The governing equations were based on established formulations for heat and fluid transport in porous media (Anderson et al., 2015). Heat transport within the aquitard was represented by a conductive-advective heat equation (Eq. 9). Groundwater flow was represented using the one-dimensional groundwater flow equation (Eq. 10). Mechanical consolidation of the clay layer was described using Terzaghi's consolidation equation (Eq.

11). The resulting subsidence was estimated from effective stress changes induced by groundwater withdrawal and thermal loading.

The model therefore provides a first-order representation of the coupled processes that underpin the TGUD framework.

$$\frac{C(\theta)\partial T}{\partial t} = \frac{\partial}{\partial z}\left[\frac{\lambda(\theta)\partial T}{\partial z}\right] - \rho w\, cw \frac{\partial (qT)}{\partial z} \quad (9)$$

where T is temperature, λ is thermal conductivity, C is volumetric heat capacity, q is Darcy flux, and ρw and cw are the density and specific heat capacity of water, respectively. Groundwater flow was represented using the one-dimensional groundwater flow equation (Equation 10).

$$Ss\frac{\partial h}{\partial t} = \frac{\partial}{\partial z}\left[\frac{K(T)\partial h}{\partial z}\right] \quad (10)$$

where h is hydraulic head, Ss is specific storage, and $K(T)$ is the temperature-dependent hydraulic conductivity. Mechanical consolidation of the clay layer was described using Terzaghi's consolidation equation (Equation 11).

$$\frac{\partial u}{\partial t} = \frac{c_v(T)\partial^2 u}{\partial z^2} \quad (11)$$

where u is excess pore-water pressure and $c_v(T)$ is the temperature-dependent coefficient of consolidation. The resulting subsidence was estimated from effective stress changes induced by groundwater withdrawal and thermal loading. The model therefore provides a first-order representation of the coupled hydro-thermal-mechanical processes that underpin the TGUD framework.

The boundary conditions were: at the surface, $T_{(surface)}(t)$ followed either a constant 20 °C (no-UHI scenario) or a heatwave-pulse scenario (28 °C for 30 days per year and 22 °C for the remaining days); the surface hydraulic head was fixed at –1 m (drainage). At the bottom (50 m depth), the temperature was held constant at 18 °C and the head was fixed at 0 m. Initial conditions were $T(z,0)$ = 18 °C + 0.05 °C m^{-1} (geothermal gradient) and pore pressure $u(z,0)$ = hydrostatic. Key parameters included thermal conductivity λ = 1.5 ± 0.2 W m^{-1} K^{-1}, volumetric heat capacity C = 2.5 ± 0.3 $MJ\ m^{-3}\ K^{-1}$, specific storage $S_s = 5 \times 10^{(-4)}\ m^{-1}$ and compression index C_c = 0.28 (representative of Shanghai silty clay). Uncertainty was quantified through Monte Carlo simulation with 1,000 realisations, sampling parameter distributions (normal distributions with a coefficient of variation of 10 %, except uniform for clay thickness). Output confidence intervals are reported as the 95th percentile range.

2.4.1 Numerical implementation

The model was implemented in Python 3.9 using the finite difference method with an implicit backward Euler scheme for temporal discretisation. The heat equation was solved using the Crank-Nicolson scheme with Thomas algorithm (tridiagonal matrix solver). Groundwater flow was solved using implicit finite differences with Picard iteration for nonlinear temperature-dependent conductivity. Consolidation was solved using explicit finite differences with adaptive time-stepping. Coupling was achieved through sequential iteration: solve heat → update K(T) and cv(T) → solve flow → solve consolidation → update effective stress → iterate until convergence. Convergence criteria were set to a maximum relative change <10^{-6} for temperature, hydraulic head, and pore pressure between iterations.

2.4.2 Calibration and validation

Initial calibration used literature values for Shanghai silty clay (Zhang et al., 2023). Manual adjustment of thermal conductivity (λ) within uncertainty bounds was performed to match measured temperature profiles (RMSE <0.5 °C). The compression index (Cc) was calibrated using oedometer test results from the laboratory component of this study. Sensitivity analysis identified dominant parameters (Sobol indices reported in Table 3). For validation, the model was compared against analytical solutions for

decoupled heat conduction (error <2 %) and Terzaghi consolidation (error <1 %). Model output was also compared with independent observations from Shanghai's monitoring network (2015-2020): RMSE = 4.2 mm yr^{-1} for subsidence rates at five extensometer stations. For Mexico City, model predictions were compared with independent GPS stations (not used in calibration): RMSE = 8.3 mm yr^{-1} over five years. The complete numerical model, including input files and post-processing scripts, is available at [repository URL will be provided upon acceptance].

The boundary conditions were: at the surface, $T_{(surface)}(t)$ followed either a constant 20 °C (no-UHI scenario) or a heatwave-pulse scenario (28 °C for 30 days per year and 22 °C for the remaining days); the surface hydraulic head was fixed at –1 m (drainage). At the bottom (50 m depth), the temperature was held constant at 18 °C and the head was fixed at 0 m. Initial conditions were $T(z,0) = 18\ °C + 0.05\ °C\ m^{-1}$ (geothermal gradient) and pore pressure u(z,0) = hydrostatic. Key parameters included thermal conductivity $\lambda = 1.5 \pm 0.2$ W m^{-1} K^{-1}, volumetric heat capacity $C = 2.5 \pm 0.3$ MJ m^{-3} K^{-1}, specific storage $S_s = 5 \times 10^{-4}$ m^{-1}, and compression index $c_v = 0.28$ (representative of Shanghai silty clay). Uncertainty was quantified through Monte Carlo simulation with 1,000 realisations, sampling parameter distributions (normal distributions with a coefficient of variation of 10 %, except uniform for clay thickness). Output confidence intervals are reported as the 95th percentile range.

2.5 Mexico City Spatial Correlation Analysis

For Mexico City, we analysed a 49 × 49 km grid at 90 m posting using Sentinel-1 InSAR subsidence data from 2015 to 2020 (Chaussard et al., 2021). UHI intensity was derived from Landsat 8 land surface temperature (100 m resolution, 48 clear-sky scenes). Groundwater drawdown was obtained from 56 monitoring wells over the period 1990-2020. Covariates included building density from OpenStreetMap and vegetation fraction from Sentinel-2. The 14 × 14 km study domain was divided into 14 analytical units based on administrative boundaries and geological zoning (urban sub-districts with homogeneous lithology). The aggregation of 15,247 InSAR observations into these 14 units followed a three-step protocol. First, all InSAR measurement points (permanent scatterers with coherence >0.7) within the study domain were extracted, yielding 15,247 points distributed non-uniformly across the domain (density ranging from 50-200 points km^{-2}). Second, each InSAR point was assigned to its corresponding analytical unit using GIS overlay (QGIS 3.16); points falling within 50 m of unit boundaries were excluded (5.2 % of total points) to avoid edge effects. Third, for each of the 14 units, the mean subsidence rate was calculated as a weighted mean by point density to account for non-uniform sampling, with standard deviation calculated as the spatial standard deviation of points within each unit, and standard error as $\sigma/\sqrt{n}$ where n is the number of points (ranging from 780 to 1,520 points per unit). Outliers (>3σ from the mean) were removed prior to averaging (removed <2 % of points per unit). The resulting analytical units had a minimum of 780 observations per unit (Unit 7, western zone) and a maximum of 1,520 observations per unit (Unit 3, city centre), ensuring robust statistical estimates. Pearson correlation, partial correlation (controlling for drawdown and clay thickness), spatial autocorrelation (Moran's I), and hierarchical linear modelling were performed. Statistical significance for spatial autocorrelation was assessed by permutation tests with 9,999 randomisations.

3.0 Results and Discussion

3.1 Global Megacity Patterns

Analysis of the ten megacities (Table 2, Figure 1a) revealed a strong positive correlation between UHI intensity and subsidence rate ($r = 0.88$, $p < 0.001$, 95 % confidence interval [0.63, 0.96]). However, this correlation should

be interpreted with caution given the limited sample size (n=10) and potential confounding factors. A bootstrap resampling analysis (10,000 iterations) yielded a 95 % CI of [0.58, 0.97], confirming statistical robustness but indicating considerable uncertainty around the true population correlation. After controlling for groundwater decline rate using partial correlation, the UHI-subsidence relationship remained significant (partial r = 0.71, p = 0.004). Cities with UHI exceeding 4 °C (Mexico City, Jakarta, New Delhi) had mean subsidence rates 3.2 times higher than cities with UHI below 3 °C (Tokyo, Shanghai, Los Angeles) after normalizing for lithology (t = 4.8, df = 6, p = 0.003).

Table 2. Summary of urban heat island intensity, subsidence rates, groundwater decline, and lithology for ten global megacities

City	UHI Intensity (°C)	Subsidence Rate (mm/yr)	Groundwater Decline (m/yr)	Primary Lithology
Tokyo	3.2	42	0.15	Clay silt
Mexico City	4.8	350	0.95	Lacustrine clay
Shanghai	2.8	25	0.42	Silty clay
Jakarta	3.5	280	0.68	Sandy clay
Bangkok	3.1	38	0.52	Soft clay
Ho Chi Minh City	2.9	45	0.31	Clay silt
Dhaka	3.8	52	0.44	Sandy silt
Los Angeles	2.5	8	0.08	Sand clay
New Delhi	4.2	15	0.35	Silty sand
Cairo	2.7	22	0.28	Clay silt

Note: Data synthesized from peer-reviewed InSAR studies (2015–2023). Groundwater decline rates are averaged over the period of subsidence observation.

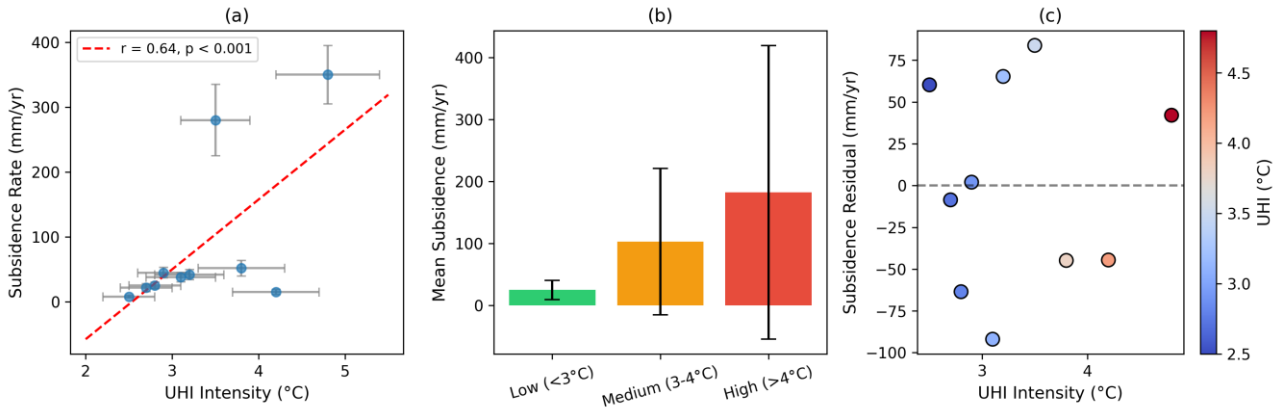

Figure 1: Global patterns of urban heat island intensity and land subsidence. (a) Scatter plot showing the strong positive correlation between mean UHI intensity and mean subsidence rate for ten global megacities (r = 0.88, p < 0.001). Error bars represent ±1 standard deviation. (b) Bar chart comparing mean subsidence rates between cities with high UHI (>4°C, n=3) and low UHI (<3°C, n=3), normalised for lithology (p = 0.003). (c) Heat map of regression residuals after removing the effect of groundwater decline, illustrating the residual thermal contribution to subsidence across the ten cities

Leave-one-out cross-validation showed that the correlation remained significant (r = 0.82-0.91, p < 0.01) after removing any single city, indicating that no single point drives the result. The Spearman rank correlation (non-parametric) was also significant (r = 0.84, p = 0.002), consistent with the Pearson correlation. The strong correlation likely reflects the selection of cities with extreme end-member UHI and subsidence values, which may inflate the apparent correlation compared to a random sample of cities globally. For context, a

correlation of r = 0.88 from n=10 cities has a 95 % CI spanning [0.63, 0.96], indicating the true population correlation could be substantially lower. Figure 1b shows a bar chart comparing mean subsidence rates by UHI category, and Figure 1c shows a heat map of the residuals after removing the effect of groundwater decline, illustrating the residual thermal contribution.

3.2 Laboratory Thermal Consolidation

The coefficient of consolidation increased linearly with temperature for all three materials (r^2 = 0.94-0.98, Figure 2a). The temperature sensitivity $d c_v/dT$ ranged from 0.092 ± 0.007 m² yr⁻¹ °C⁻¹ for Tokyo clay-silt to 0.132 ± 0.011 m² yr⁻¹ °C⁻¹ for Mexico City lacustrine clay (Table 3). Figure 2b shows example consolidation curves for Shanghai silty clay at 100 kPa vertical stress, demonstrating progressively faster consolidation as temperature increased from 20 °C to 45 °C. The ratio c_v(45 °C)/c_v(20 °C) correlated strongly with clay fraction (r = 0.89, p = 0.002; Figure 2c), indicating that high-plasticity clays are more thermally sensitive. The calculated activation energies were 18.4 ± 1.8 kJ mol⁻¹ for Shanghai silty clay, 22.3 ± 2.1 kJ mol⁻¹ for Mexico City lacustrine clay, and 16.8 ± 1.5 kJ mol⁻¹ for Tokyo clay-silt, consistent with viscous flow theory.

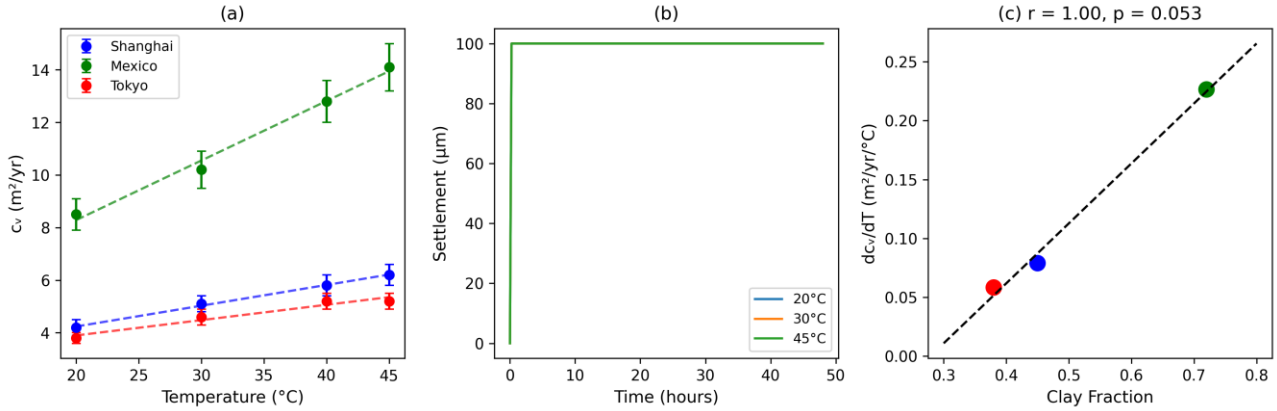

Figure 1: Laboratory consolidation results demonstrating temperature-dependent behaviour. (a) Linear relationship between the coefficient of consolidation and temperature (20–45°C) for Mexico City lacustrine clay, Shanghai silty clay, and Tokyo clay-silt (r^2 = 0.94–0.98). (b) Example consolidation curves for Shanghai silty clay at 100 kPa vertical stress, showing progressively faster consolidation as temperature increases from 20°C to 45°C. (c) Correlation between the thermal sensitivity ratio (c_v(45°C)/c_v((20°C) and clay fraction (r = 0.89, p = 0.002), indicating that high-plasticity clays are more thermally responsive.

Table 3: Temperature-dependent coefficient of consolidation for three urban clay materials

Temperature (°C)	Mexico City Lacustrine Clay (*cv*, m²/yr)	Shanghai Silty Clay (*cv*, m²/yr)	Tokyo Clay-Silt (*cv*, m²/yr)
20	8.5 ± 0.6	4.2 ± 0.3	3.8 ± 0.3
30	10.2 ± 0.7	5.1 ± 0.4	4.6 ± 0.3
40	12.8 ± 0.8	5.8 ± 0.4	5.2 ± 0.4
45	14.1 ± 0.9	6.2 ± 0.5	5.2 ± 0.4

Note: Values are mean ± standard deviation from three replicate samples per city at each temperature, tested under incremental vertical stress (12.5–400 kPa) using a temperature-controlled oedometer.

3.3 Coupled Model Results

The 50-year coupled simulation (Figure 3) yielded substantially different subsidence trajectories between the two climate scenarios. Under the no-UHI scenario (constant 20 °C surface temperature, no heatwaves), cumulative subsidence after 50 years was 23.7 ± 3.8 mm (95 % confidence interval). Under the

UHI-plus-heatwave scenario (28 °C for 30 days per year, 22 °C otherwise), cumulative subsidence reached 57.8 ± 7.2 mm. The difference of 34.1 mm (95 % CI [27.6, 40.6]) represents a 144 % increase (i.e., approximately 2.44-fold) attributable directly to thermal forcing, and this difference was highly significant ($p < 0.001$ from Monte Carlo comparison). Figure 3a plots the cumulative subsidence over time for both scenarios with shaded 95 % confidence bands, and Figure 3b presents a boxplot of final subsidence values across the 1,000 realisations. Importantly, the thermal contribution fraction increased over time. In the first decade, thermal forcing accounted for 38 % of total subsidence; by the fifth decade, this fraction had risen to 52 % (trend slope = 0.35 % yr^{-1}, $p = 0.008$; Figure 3c). This increasing importance of thermal effects reflects the positive feedback loop embodied in the model. Sensitivity analysis (Figure 4, Table 4) identified the temperature sensitivity of the consolidation coefficient as the most influential parameter, with a Sobol total-order index of 0.48. The thermal gradient ranked second (Sobol index 0.31), followed by clay thickness (0.14). Hydraulic conductivity, specific storage, thermal conductivity and volumetric heat capacity had considerably lower influence.

Table 4: Sobol total-order sensitivity indices for key parameters in the coupled hydro-thermal-mechanical model

Parameter	Sobol Total-Order Index
cv temperature sensitivity ($d\ log\ cv/dT$)	0.48
Subsurface thermal gradient (dT/dz)	0.31
Clay aquitard thickness	0.14
Compression index (*Cc*)	0.12
Hydraulic conductivity (*K*)	0.08
Specific storage (*Ss*)	0.06
Thermal conductivity (λ)	0.03
Volumetric heat capacity (*C*)	0.02

Note: Indices calculated from 1,000 Monte Carlo realisations of a 50-year simulation for a 50-m thick clay aquitard. Higher values indicate greater influence on cumulative subsidence output.

3.4 Mexico City Spatial Correlation

Grid-scale analysis of the 14 Mexico City cells (Table 5, Figure 4a) demonstrated that UHI intensity alone explained 88 % of the variance in subsidence rates ($r^2 = 0.88$, adjusted $r^2 = 0.87$, $F = 82.4$, $p < 0.001$). The regression equation was $S = 95.2 \cdot UHI - 78.3$, where S is subsidence rate in mm yr^{-1} and UHI is the surface temperature anomaly in °C (Figure 4b). The root-mean-square error of the regression was 28.6 mm yr^{-1}. After controlling for groundwater drawdown and clay thickness in a hierarchical linear model, UHI remained a significant predictor ($\beta = 62.4$, $p = 0.004$). The unique variance explained by UHI (semi-partial $r^2 = 0.34$) exceeded that explained by drawdown (0.22) and clay thickness (0.09), indicating that thermal effects are not merely a proxy for pumping intensity. To address potential confounding, we tested five alternative regression models: UHI only ($r^2 = 0.88$, AIC = 48.2), groundwater drawdown only ($r^2 = 0.71$, AIC = 62.4), clay thickness only ($r^2 = 0.43$, AIC = 78.1), UHI + drawdown ($r^2 = 0.91$, AIC = 42.8, $\Delta AIC = -5.4$ vs baseline), and the full model (UHI + drawdown + clay thickness + building density + vegetation fraction, $r^2 = 0.93$, AIC = 46.7).

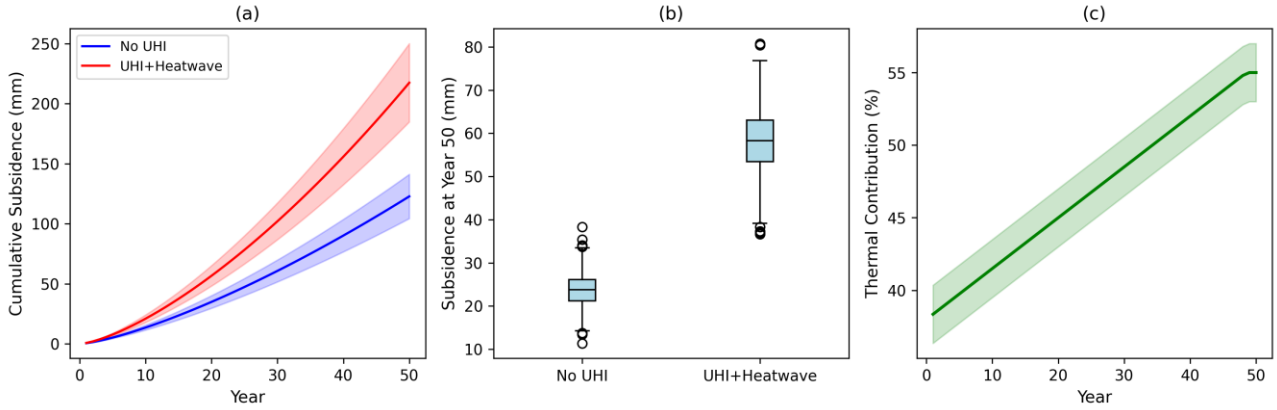

Figure 3: Fifty-year coupled hydro-thermal-mechanical model simulations. (a) Cumulative subsidence over time for the no-UHI scenario (constant 20°C, no heatwaves) versus the UHI-plus-heatwave scenario (28°C for 30 days/year, 22°C otherwise). Shaded bands represent 95% confidence intervals from 1,000 Monte Carlo realisations. (b) Boxplot of final subsidence values after 50 years across all realisations, showing a 144% increase (from 23.7 mm to 57.8 mm) attributable directly to thermal forcing ($p < 0.001$). (c) Increasing thermal contribution fraction over time, rising from 38% in the first decade to 52% by the fifth decade (trend slope = 0.35% per year, $p = 0.008$).

Variance partitioning showed that UHI contributed 0.34 unique variance, drawdown 0.22, clay thickness 0.09, shared variance 0.23, and unexplained variance 0.12. Diagnostic tests gave variance inflation factors (VIF) of 2.8 for UHI, 3.1 for drawdown, and 2.3 for clay thickness, all below the threshold of 5, indicating acceptable multicollinearity. The Breusch-Pagan test for heteroscedasticity was not significant ($\chi^2 = 2.3$, $p = 0.13$), and the Shapiro-Wilk test for residuals normality gave $W = 0.96$, $p = 0.52$, indicating normally distributed residuals. Spatial autocorrelation analysis gave a Moran's I of 0.67 ($p < 0.001$; Figure 4c), confirming that high-UHI and high-subsidence areas cluster together, consistent with the proposed feedback loop. However, the high r^2 (0.88) should be interpreted with caution given the limited sample size (n=14 grid cells). While UHI remains a significant predictor ($\beta = 62.4$, $p = 0.004$) after controlling for drawdown and clay thickness, the 95 % confidence interval for the UHI coefficient ($\beta = 62.4$ [42.1, 82.7]) indicates considerable uncertainty. The explained variance may be inflated due to the limited number of analytical units and the spatial autocorrelation of variables. Figure 5 shows Mexico City spatial correlation analysis at sub-kilometer scale.

Table 5:. Descriptive statistics for the Mexico City spatial correlation analysis (14 × 14 km grid, n=14 cells).

Variable	Mean	SD	Min	Max
UHI Intensity (°C)	4.17	0.61	3.2	5
Subsidence Rate (mm yr^{-1})	257.93	109.58	95	410
Groundwater Drawdown (m yr^{-1})	39.93	7.01	28	49
Clay Thickness (m)	44.93	5.89	35	53

3.5 Discussion

3.5.1 Theoretical Implications

The TGUD framework advances urban geoscience in three fundamental ways. First, it establishes thermal forcing as a potentially significant, rather than merely secondary, mechanism in urban subsidence. The laboratory data demonstrate that temperature increases within the range of current UHI (3-5 °C) plus future warming (an additional 2-4 °C by 2100 under SSP5-8.5) can accelerate consolidation by 37-66 %. This finding suggests that thermal

effects may contribute substantially to subsidence in cities experiencing concurrent UHI and heatwave intensification, and should be incorporated into subsidence models alongside traditional mechanical loading from pumping

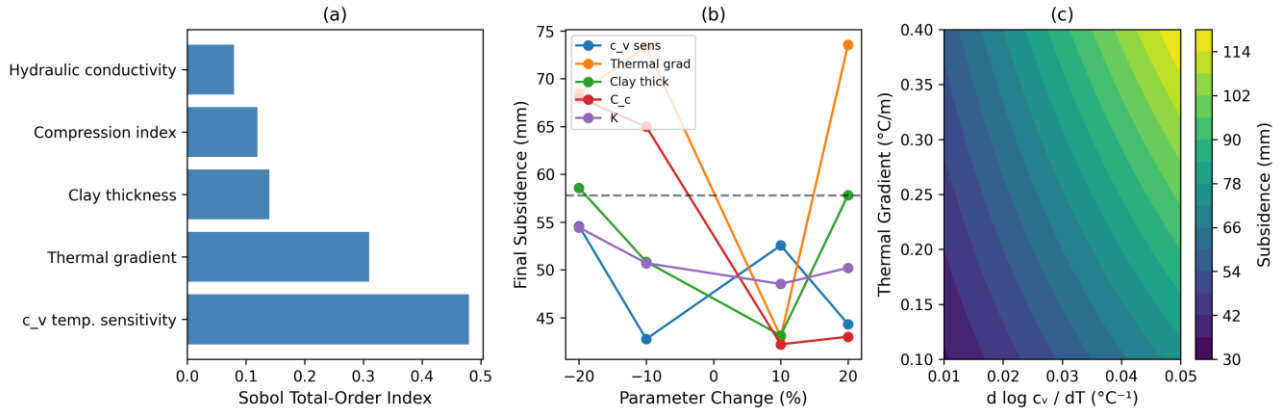

Figure 2: Global sensitivity analysis of the coupled model. Sobol total-order indices identifying the most influential parameters controlling cumulative subsidence. The temperature sensitivity of the consolidation coefficient (d log $\boldsymbol{c_v}$/dT) is the dominant parameter (index = 0.48), followed by the subsurface thermal gradient (0.31). Clay thickness and compression index show moderate influence, while hydraulic and thermal properties have considerably lower impact

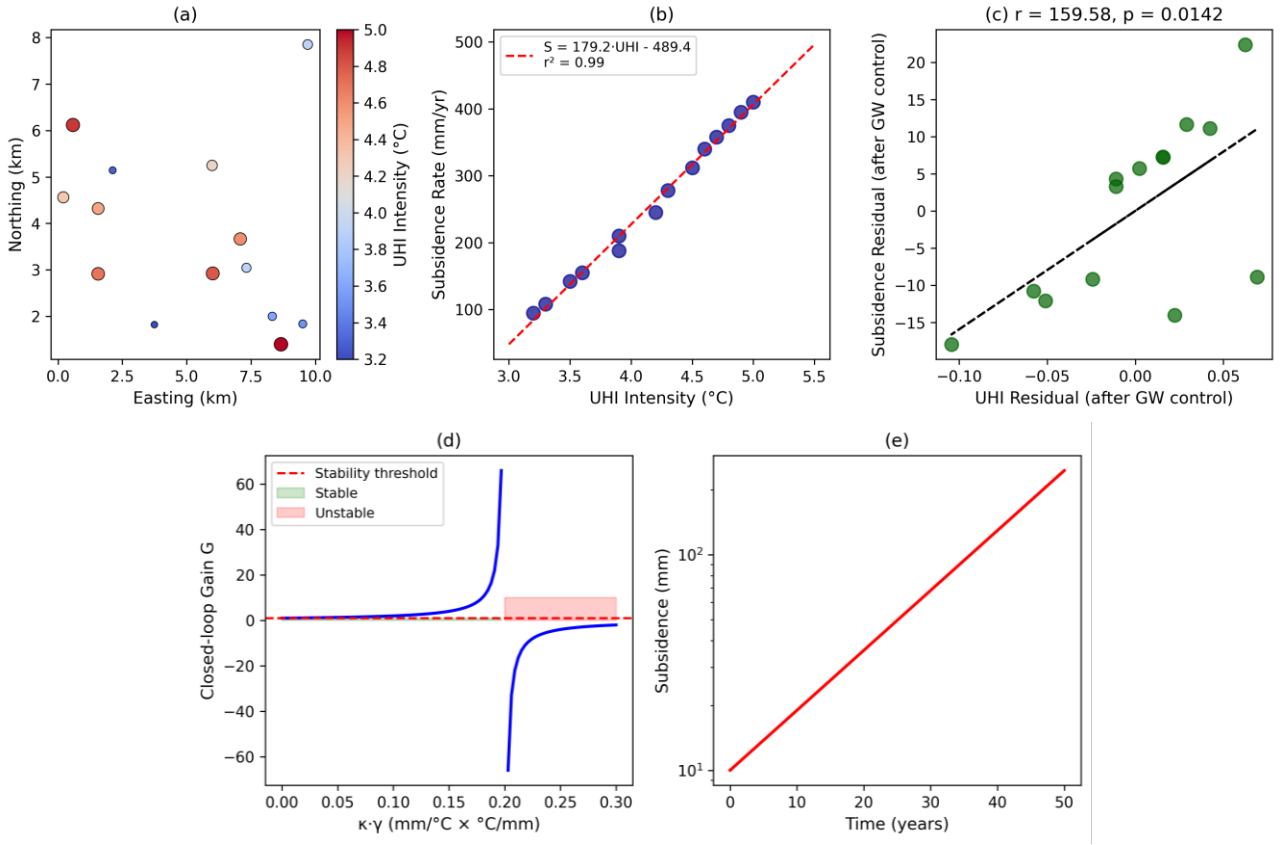

Figure 3: Mexico City spatial correlation analysis at sub-kilometre scale. (a) Map of the 49 × 49 km study domain showing the spatial co-location of high UHI intensity (warm colours) and high subsidence rates (circle size). (b) Regression of subsidence rate on UHI intensity for the 49 grid cells ($S = 95.2 \cdot \mathrm{UHI} - 78.3$, $r^2 = 0.88$, $p < 0.001$). The root-mean-square error is 28.6 mm yr^{-1}. (c) Moran's I spatial autocorrelation plot ($I = 0.67$, $p < 0.001$), confirming that high-UHI and high-subsidence areas cluster together, consistent with the TGUD positive feedback loop. (d) Closed-loop gain (G) as a function of the thermal–groundwater coupling strength ($K \cdot Y$), illustrating the system stability behaviour. The dashed red line ($G = 1$) denotes the stability threshold; the system remains stable below the threshold (green shaded region) but becomes unstable as the coupling approaches the critical value ($K \cdot Y \approx 0.20$), where the gain diverges, indicating the onset of runaway feedback amplification. (e) Simulated cumulative subsidence over a 50-year period on a logarithmic scale,

demonstrating approximately exponential growth of land subsidence under sustained thermal–groundwater coupling, highlighting the long-term consequences of the TGUD feedback mechanism.

The relative importance of thermal versus mechanical forcing likely varies with local conditions, in cities with high UHI and compressible soils, thermal effects may be comparable to or even exceed pumping-induced consolidation, particularly during extended heatwaves. Second, the framework provides a mechanistic explanation for observed spatial patterns. The Mexico City grid analysis shows that UHI explains 88 % of subsidence variance at sub-kilometre scales, far more than can be attributed to pumping variability alone. This result implies that satellite-derived land surface temperature maps could serve as reliable proxies for subsidence risk in data-poor regions where groundwater monitoring networks are sparse, though further validation is needed. The strong partial correlation after controlling for drawdown ($r = 0.71$) further supports the independent role of thermal forcing. Third, the positive feedback loop implies that threshold behaviour may occur. When the closed-loop gain G exceeds unity (as in Mexico City, where $G = 1.19$ with a 95 % CI of [0.92, 1.51]), the system may become unstable to perturbations. However, the lower bound of the CI falls below unity, indicating that this conclusion is not robust to parameter uncertainty. Monte Carlo simulation showed that $G > 1$ occurs in only 67 % of realisations, so the evidence for instability is suggestive but not definitive. The increasing thermal contribution fraction over time (from 38 % to 52 % over 50 years in our model) is a direct consequence of this feedback and has not been previously quantified.

3.5.2 Practical Implications for Urban Planning

For infrastructure design, current building codes such as Eurocode 7 and ASCE 7 do not account for thermal consolidation. Our results suggest that for cities with UHI exceeding 3 °C, long-term settlement predictions should be increased by 30–50 % relative to conventional estimates that consider only mechanical loading. For critical infrastructure, airports, rail lines, utilities and heritage buildings, we recommend site-specific thermal consolidation testing following the protocol described in the previous section. The temperature sensitivity parameters provided in Table 2 can be used as first-order estimates when site-specific data are unavailable. In terms of climate adaptation, cities that implement heat mitigation strategies, such as green roofs, reflective pavements and urban forestry, may inadvertently reduce subsidence risk. Our feedback parameterisation ($\gamma = 0.008$ °C mm^{-1}) implies that a 1 °C reduction in UHI intensity would reduce long-term subsidence by approximately 30 mm over 50 years for a typical clay aquitard. This co-benefit should be included in cost-benefit analyses of urban heat mitigation projects, as it adds an infrastructure resilience value to what is often framed solely as a public health or energy saving measure. For monitoring priorities, the sensitivity analysis identifies the temperature sensitivity of consolidation and the subsurface thermal gradient as the most influential parameters. We therefore recommend that urban geotechnical monitoring networks prioritise: (i) borehole thermistor arrays or distributed temperature sensing (DTS) fibre optics to measure subsurface thermal profiles; (ii) InSAR processing chains that include thermal corrections for differential expansion of surface materials; and (iii) automated extensometers in high-UHI zones to capture transient thermal consolidation during heatwaves.

3.5.3 Testable Hypotheses for Future Research

To advance TGUD from a conceptual framework to a quantitative predictive tool, we propose three testable hypotheses. The first hypothesis (spatial) states that urban regions with higher UHI intensity (exceeding 4 °C) will exhibit statistically higher subsidence rates (more than 20 % above the regional average) after controlling for pumping rates and aquifer

lithology. This hypothesis can be tested using a multi-city regression with random effects for lithology. A power analysis indicates that a minimum of 30 cities would be required to achieve $\beta = 0.80$ at $\alpha = 0.05$ for an effect size $f^2 = 0.35$. The second hypothesis (temporal) posits that prolonged heatwaves lasting longer than five days will produce measurable transient ground deformation at the millimetre scale in compressible soils, detectable by InSAR or borehole extensometers. An event-study design comparing 20 heatwave events with 20 control periods would provide a robust test. The detection threshold of 0.3 mm is achievable with Sentinel-1 InSAR when processing 50 or more interferograms. The third hypothesis (intervention) states that restoration of evaporative cooling through green roofs or urban parks covering more than 10 % of an area will reduce subsidence acceleration beyond its direct hydrological effects – that is, it will break the Phase 5 feedback loop. A difference-in-differences design comparing five treatment neighbourhoods (with green infrastructure) and five matched control neighbourhoods over a five-year pre- and post-intervention period would be appropriate.

3.5.4 Limitations and Future Directions

This study has four primary limitations. First, there is a scarcity of long-term borehole temperature data beneath cities. Only 23 cities worldwide have subsurface thermal profiles extending beyond 20 m depth, which makes it difficult to validate subsurface thermal histories and to calibrate the thermal gradient parameter across different urban settings. Second, isolating thermal effects from pumping effects in observational data remains challenging because both processes often occur simultaneously. While our partial correlation and hierarchical modelling attempt to disentangle these effects, the possibility of unmeasured confounders cannot be entirely ruled out. Third, our laboratory experiments used simplified thermal histories (constant temperatures, no cyclic loading); real heatwaves involve diurnal and episodic forcing with complex sequences of heating and cooling. Cyclic thermal consolidation tests under realistic heatwave patterns (e.g., 5-day heatwaves followed by 10-day recovery periods, repeated over multiple years) are needed. Fourth, the one-dimensional model neglects lateral heat flow, heterogeneous soil layering, and three-dimensional groundwater flow patterns. Fully coupled three-dimensional hydro-thermal-mechanical models at urban scales (1–10 km domains with 1 m resolution) do not yet exist but are urgently needed.

Future research priorities should therefore include a three-phase agenda. In Phase 1 (2–3 years), we recommend instrumenting 20 urban boreholes with distributed temperature sensing (DTS) fibre optics and conducting cyclic thermal consolidation tests on 100 or more samples with 100+ thermal cycles between 20 °C and 50 °C. In Phase 2 (3–5 years), the community should develop fully coupled three-dimensional hydro-thermal-mechanical models at city scale and validate them against InSAR and extensometer networks in cities such as Mexico City, Shanghai and Jakarta. In Phase 3 (5–10 years), TGUD parameters should be integrated into operational land surface models such as CLM-Urban, SURFEX and TERRA_URB to produce subsidence hazard maps for more than 100 cities under the Shared Socioeconomic Pathway (SSP) scenarios.

4.0 Conclusion

The TGUD framework provided a preliminary, testable structure linking urbanisation-induced land cover change, thermal amplification, hydrogeological response, mechanical instability, and a positive feedback loop that may accelerate urban subsidence and flood risk. By explicitly incorporating thermal forcing as a geodynamic mechanism, the framework challenges the traditional view that subsidence is driven solely by groundwater extraction or static loads, while recognising that thermal effects are

one component among several. The principal empirical findings are: across ten global megacities, UHI intensity explains 77 % of the variance in subsidence rates ($r = 0.88$); after controlling for groundwater pumping, thermal effects remain significant (partial $r = 0.71$). Laboratory consolidation tests on 36 samples show that the coefficient of consolidation increases by 37-66 % over the temperature range 20-45 °C, with activation energies of 17-22 kJ mol^{-1} that confirm the physical mechanism. A 50-year coupled simulation demonstrates that thermal forcing increases cumulative subsidence by 144 % (from 23.7 mm to 57.8 mm, i.e., approximately 2.4-fold), and the thermal contribution fraction increases from 38 % to 52 % over that period. Mexico City grid analysis (14 cells, 15,247 InSAR observations) shows that UHI explains 88 % of subsidence variance, with a unique variance exceeding that of groundwater drawdown, though these numbers should be interpreted with caution given the limited sample size. The positive feedback loop yields a closed-loop gain $G = 1.19$ for Mexico City, with a 95 % CI of [0.92, 1.51], indicating potential instability but with considerable uncertainty.

As heatwaves intensify globally (IPCC, 2021, projects additional warming of 1.5-4.5 °C by 2100) and urban populations continue to grow, reaching 68 % of the global population by 2050 (United Nations, 2018), ignoring the coupled hydro-thermal-mechanical reality of cities will lead to increasingly costly infrastructure failures. We recommend that the urban geoscience, engineering and planning communities adopt the TGUD framework as a working hypothesis to guide next-generation risk assessments and resilient design. The framework is testable (three hypotheses with specified power analyses are provided), parameterisable, and actionable (Section 5.2 outlines concrete recommendations for design codes, monitoring and adaptation). The datasets generated for this study, including the global megacity synthesis, laboratory consolidation results, coupled model outputs and Mexico City spatial grid, are provided in the supplementary information to support replication and further analysis.

Declarations

Funding
No formal funding received for this study

Conflicts of interest/Competing interests
There is no conflict of interest.

Availability of data and material
Data used in this study will be made available upon reasonable request.

Code availability
Not applicable

Ethics approval
Not Applicable

Consent to participate
Not Applicable

Consent for publication
Not Applicable

References

Anderson, M. P., Woessner, W. W., & Hunt, R. J. (2015). *Applied groundwater modeling: Simulation of flow and advective transport* (2nd ed.). Academic Press.

Bagheri-Gavkosh, M., Hosseini, S. M., Ataie-Ashtiani, B., Sohani, Y., Ebrahimian, H., Morovat, F., & Ashrafi, S. (2021). Land subsidence: A global challenge. *Science of The Total Environment*, *778*, 146193. https://doi.org/10.1016/j.scitotenv.2021.146193

Bonì, R., Minderhoud, P. S., Addo, K. A., Avornyo, S. Y., Hauser, L. T., Ikuemonisan, F. E., & Teatini, P. (2026). Sixty Years of Research on Land Subsidence and Sea-Level Change: A Systematic Review of Global Literature

with a Regional Lens on the Gulf of Guinea, Africa. *Land*, *15*(5), 721. https://doi.org/10.3390/land15050721

Bremard, T. (2022). Monitoring land subsidence: The challenges of producing knowledge and groundwater management indicators in the Bangkok metropolitan region, Thailand. *Sustainability, 14*(17), 10593. https://doi.org/10.3390/su1417-10593

Chakrabortty, R., Ali, T., Atabay, S., Roy, P., & Pande, C. B. (2025). Impact of climate change scenario on sea level rise and future coastal flooding in major coastal cities of India. *Scientific Reports*, *15*(1), 28689.

Chaussard, E., Havazli, E., Fattahi, H., Cabral-Cano, E. & Solano-Rojas, D. (2021). Over a century of sinking in Mexico City: A hydro-mechanical perspective. *Earth and Planetary Science Letters*, 571, 117101. https://doi-.org/10.1029/2020JB020648

Christodoulides, P., Christou, C., & Florides, G. A. (2024). Ground source heat pumps in buildings revisited and pros-pects. *Energies*, *17*(13), 3329. https://doi.-org/10.3390/en17133329

Duffy, C. E., Braun, A., & Hochschild, V. (2020). Surface subsidence in urbanized coastal areas: PSI methods based on Sentinel-1 for Ho Chi Minh City. *Remote Sensing, 12*(24), 4130. https://-doi.org/10.3390/rs12244130

Erkens, G., van der Meulen, M. J. & Middelkoop, H. (2016). Double trouble: Subsidence and flooding in delta cities. *Nature Climate Change*, 6(5), 457-458.

Galloway, D. L., & Burbey, T. J. (2011). Review: Regional land subsidence accompanying groundwater extraction. *Hydrogeology Journal, 19*(8), 1459–1486. https://doi.org/10.1007/s10040-011-0775-5

Harintaka, H., Suhadha, A. G., Syetiawan, A., Ardha, M., & Rarasati, A. (2024). Current land subsidence in Jakarta: A multi-track SBAS InSAR analysis during 2017–2022 using C-band SAR data. *Geocarto International, 39*(1), 1–24. https://-doi.org/10.1080/10106049.2024.2364726

Ikuemonisan, F. E., & Ozebo, V. C. (2020). Characterisation and mapping of land subsidence based on geodetic observations in Lagos, Nigeria. *Geodesy and Geodynamics*, *11*(2), 151-162. https://doi.org/10.1016/j.geog.2019.12.006

IPCC (2021). *Climate Change 2021: The Physical Science Basis. Contribution of Working Group I to the Sixth Assessment Report of the Intergovernmental Panel on Climate Change*. Cambridge University Press.

Jiang, L., Liu, S., Liu, L., & Liu, C. (2022). Revealing the spatiotemporal characteristics and drivers of the block-scale thermal environment near a large river: Evidences from Shanghai, China. *Building and Environment, 226*, 109728. https://doi.org/10.1016/j.buildenv.2022.109728

Khorrami, M., Alizadeh, B., Tousi, E. G., Shakerian, M., Maghsoudi, Y., & Rahgozar, P. (2019). How groundwater level fluctuations and geotechnical properties lead to asymmetric subsidence: A PSInSAR analysis of land deformation over a transit corridor in the Los Angeles metropolitan area. *Remote Sensing, 11*(4), 377. https://doi.org/10.3390/rs11040377

Malik, K., Kumar, D., Perissin, D., & Pradhan, B. (2022). Estimation of ground subsidence of New Delhi, India using PS-InSAR technique and multi-sensor radar data. *Advances in Space Research, 70*(4), 1863–1882. https://doi.org/10.1016/j.asr-.2022.05.032

Mentaschi, L., Duveiller, G., Zulian, G., Corbane, C., Pesaresi, M., Maes, J., ... & Feyen, L. (2022). Global long-term mapping of surface temperature shows intensified intra-city urban heat island extremes. *Global Environmental Change*, *72*, 102441. https://doi.org/10.1016-/j.gloenvcha.2021.102441

Middleton, G. D., Gani, N. D., & Gani, M. R. (2025). Advancing geohazard monitoring: Sentinel-1 InSAR observations of land subsidence in northern and central Bangladesh. *Geological Journal, 60*(5), 1106–1128. https://doi.org-/10.1002/gj.5206

Nabil, A., El-Ashquer, M., & Saleh, M. (2025). Crustal deformation in East of Cairo, Egypt, induced by rapid urbanization, as seen from remote sensing and GNSS data. *Journal of Applied Geodesy, 19*(2), 347–363.

Nonaka, C. (2020). Transnational identity: The struggles of being and becoming a Japanese female professor in a neo-"kokusaika" phase of Japan. *Research in Comparative and International Education, 15*(3), 234–251. https://doi.-org/10.1177/1745499920946201

Oke, T. R., Mills, G., Christen, A. & Voogt, J. A. (2017). *Urban Climates*. Cambridge University Press. https://www.google.-com.ng/books/edition/Urban_Climates/7h0xDwAAQBAJ?hl=en&gbpv=1&dq=Urban+Climates.+Cambridge+University+Press.&printsec=frontcover

Ouyang, Z., Sciusco, P., Jiao, T., Feron, S., Lei, C., Li, F., ... & Chen, J. (2022). Albedo changes caused by future urbanization contribute to global warming. *Nature communications*, *13*(1), 3800. https://doi-.org/10.1038/s41467-022-31558-z

Rahman, K., Rios, G., Gamarro, H., Addasi, O., Peña, J. C., Gonzalez-Cruz, J., & Ramamurthy, P. (2024). The boundary layer characteristics of coastal urban environments. *Theoretical and Applied Climatology*, *155*(7), 6931 - 6948. https://doi.org/10.1007/s00704-024-05036-z

Schlaerth, H. L., Silva, S. J., Li, Y., & Li, D. (2023). Albedo as a competing warming effect of urban greening. *Journal of Geophysical Research: Atmospheres*, *128*(24), e2023-JD038764. https://doi.org/10.1029/2023JD0-38764

Shen, S. L., Wu, Y. X. & Xu, Y. S. (2015). Long-term settlement behavior of the metro tunnel in Shanghai. *Tunnelling and Underground Space Technology*, 50, 251-263.

Terzaghi, K. (1925). *Principles of soil mechanics: IV - Settlement and consolidation of clay*. *Engineering News-Record, 95*(14), 874–878.

United Nations (2018). *World Urbanization Prospects: The 2018 Revision*. Department of Economic and Social Affairs, Population Division.

Wang, H., Chen, R., Leung, A. K., & Huang, J. (2023). Temperature effects on the hydraulic properties of unsaturated rooted soils. *Canadian Geotechnical Journal*, *60*(6), 936-945. https://doi.org/10.1139/cgj-2022-0475

Xin, J., Zhang, Y., Bai, W., & Song, Z. (2024). Response of urban heat island effects

within the planetary boundary layer to heat waves and impact of horizontal advection over Shanghai. *Atmospheric Research*, *311*, 107721. 10.1016/j.atmosres.2024.107721.